

AMI Galactic Plane Survey at 16 GHz: I – Observing, mapping and source extraction*

AMI Consortium: Yvette C. Perrott^{1†}, Anna M. M. Scaife², David A. Green¹, Matthew L. Davies¹, Thomas M. O. Franzen³, Keith J. B. Grainge^{1,4}, Michael P. Hobson¹, Natasha Hurley-Walker⁵, Anthony N. Lasenby^{1,4}, Malak Olamaie¹, Guy G. Pooley¹, Carmen Rodríguez-Gonzálvez⁶, Clare Rumsey¹, Richard D. E. Saunders^{1,4}, Michel P. Schammel¹, Paul F. Scott¹, Timothy W. Shimwell³, David J. Titterington¹, Elizabeth M. Waldram¹

¹ Astrophysics Group, Cavendish Laboratory, 19 J. J. Thomson Avenue, Cambridge CB3 0HE

² School of Physics and Astronomy, University of Southampton, Highfield, Southampton, SO17 1BJ

³ CSIRO Astronomy & Space Science, Australia Telescope National Facility, PO Box 76, Epping, NSW 1710, Australia

⁴ Kavli Institute for Cosmology Cambridge, Madingley Road, Cambridge CB3 0HA

⁵ International Centre for Radio Astronomy Research, Curtin Institute of Radio Astronomy, 1 Turner Avenue, Technology Park, Bentley, WA 6845, Australia

⁶ Spitzer Science Center, MS 220-6, California Institute of Technology, Pasadena, CA 91125 USA

Accepted ??. Received ??.

ABSTRACT

The AMI Galactic Plane Survey (AMIGPS) is a large area survey of the outer Galactic plane to provide arcminute resolution images at milli-Jansky sensitivity in the centimetre-wave band. Here we present the first data release of the survey, consisting of 868 deg² of the Galactic plane, covering the area $76^\circ \lesssim \ell \lesssim 170^\circ$ between latitudes of $|b| \lesssim 5^\circ$, at a central frequency of 15.75 GHz (1.9 cm). We describe in detail the drift scan observations which have been used to construct the maps, including the techniques used for observing, mapping and source extraction, and summarise the properties of the finalized datasets. These observations constitute the most sensitive Galactic plane survey of large extent at centimetre-wave frequencies greater than 1.4 GHz.

Key words: catalogues – surveys – ISM: general – radio continuum: general – Galaxy: general

1 INTRODUCTION

Large-area radio surveys contribute to our understanding of the Universe in numerous and diverse ways. Discoveries from these surveys have become key ingredients of modern astrophysics: pulsars, radio galaxies, quasars and more (see e.g. Longair 1998). For studies of our Galaxy, radio surveys are particularly beneficial as the longer wavelength radio emission does not suffer from the same extinction and opacity effects as optical and infra-red surveys and the dense regions of dust and gas which dominate the low-latitude Galactic plane become largely transparent, allowing us to study sources in these regions. However, the bulk of Galactic radio surveys are at frequencies at or below 1.4 GHz and as such are nec-

essarily biased against objects whose spectra rise with frequency, such as dense star-forming regions. Two examples of the need for higher-frequency, centimetre-wave Galactic surveying are as follows.

The first is the hypercompact HII (HCHII) region. Thought to indicate the earliest visible stage of massive star formation, these objects are two orders of magnitude more dense than the better known ultracompact (UCHII) region and have steeply rising spectra. HCHII regions were discovered serendipitously in observations of UCHII, having been missed previously in their entirety by Galactic plane surveys concentrated at $\nu < 5$ GHz. The turnover frequency between the optically thick and thin regimes for thermal bremsstrahlung is a linear function of emission measure (e.g. Mezger & Henderson 1967) causing such low frequency surveys (e.g. $\nu \leq 5$ GHz) to preferentially select against dense plasmas ($n_e \leq 10^{11} \text{ m}^{-3}$). Such plasmas are not limited to HCHII regions

* We request that any reference to this paper cites ‘AMI Consortium: Perrott et al. 2012’

† Issuing author: email – ycp21@mrao.cam.ac.uk

but also include a variety of other Galactic objects such as massive stellar winds, ionised jets from young stellar objects (e.g. Anglada 1995) and young planetary nebulae (e.g. Bains et al. 2009).

The second is the anomalous microwave emission (AME), now being identified in an increasing number of Galactic objects, that was missed in low frequency Galactic surveys. First identified by CMB experiments (Leitch et al. 1997) as a large scale foreground contaminant this form of emission has since been demonstrated to exist in more compact objects such as dark (e.g. Casassus et al. 2006; AMI Consortium: Scaife et al. 2009; Scaife et al. 2010) and molecular clouds (Watson et al. 2005; Tibbs et al. 2011). Although multiple mechanisms have been proposed to explain AME, dipole emission from rapidly rotating very small dust grains (Draine & Lazarian 1998a, Draine & Lazarian 1998b) is generally considered to be most likely. Such spinning dust emission has a sharply peaked SED with a maximum in the frequency range 10 – 50 GHz depending on grain size distributions.

A current lack of surveys in this frequency range means that our knowledge of the overall properties of objects which exhibit emission from spinning dust, objects which are characterized by dense plasmas, and indeed the global distribution of rising-spectrum emission in the Galaxy, is extremely poor. Those surveys which are available, such as the 9C Ryle Telescope survey (15 GHz; Waldram et al. 2003), the GPA survey (14.35 GHz; Langston et al. 2000) and the AT20G survey (20 GHz; Murphy et al. 2010) have provided us with tantalising insights into the high frequency Galactic plane, but there is a continuing need for higher sensitivity, resolution and sky area coverage at these frequencies.

The interferometric Arcminute Microkelvin Imager (AMI) Galactic Plane Survey (AMIGPS) provides the most sensitive centimetre-wave Galactic plane survey of large extent at $\nu > 1.4$ GHz. AMIGPS is a drift-scan survey of the northern Galactic plane at ≈ 16 GHz, covering (in the first data release) the region $76^\circ \lesssim \ell \lesssim 170^\circ$ and $|b| \lesssim 5^\circ$. The AMI Small Array (SA) has been used for the survey since its relatively large field of view (≈ 400 arcmin 2) makes covering large areas feasible, and its short baselines mean that extended objects, very common in the Galaxy, are at least partially observable. The resolution of the survey is ≈ 3 arcmin and the noise level is ≈ 3 mJy beam $^{-1}$ away from bright sources.

This paper focuses on the techniques employed for observing (Section 3), mapping (Section 4) and source extraction (Section 5) in the AMIGPS. The positional and flux density calibration accuracy of the survey are also tested in Section 6, and in Section 7 the maps and catalogue are described. In a following paper, hereafter Paper II, the first results from the survey, including the follow-up of rising-spectrum objects in order to detect U/HCH $_{\text{II}}$ regions, will be presented.

2 THE ARCMINUTE MICROKELVIN IMAGER SMALL ARRAY

The AMI (AMI Consortium: Zwart et al. 2008) was designed as a Sunyaev-Zel'dovich (SZ) effect instrument, and consists of two separate instruments: the Small Array (SA), optimised for observing extended SZ decrements on arcminute scales, and the Large Array (LA) with higher resolution (30 arcsec), used for characterising and subtracting point source foregrounds from SA data. The AMIGPS was carried out solely with the SA, although some follow-up observations were also made using the LA; these latter

will be used as calibration accuracy checks in Section 6 and will be described fully in Paper II.

The SA is an interferometer array comprising ten 3.7-metre-diameter, equatorially-mounted dishes, with a range of baselines of 5 – 20 m. It operates at frequencies over 13.9 – 18.2 GHz with the passband divided into six channels of 0.72-GHz bandwidth. It has a primary beam at the central frequency of 15.75 GHz of ≈ 20 arcmin full width at half-maximum (FWHM) and a typical synthesised beam FWHM of ≈ 3 arcmin (this varies depending on the precise uv -coverage of any observation). The telescope measures a single, linear polarisation (Stokes $I + Q$) and has a flux-density sensitivity of ≈ 30 mJy s $^{-1/2}$. It is sensitive to angular scales of up to ≈ 10 arcmin (depending on the uv -coverage).

3 OBSERVATIONS

The AMIGPS is observed in drift-scan mode, in which the SA is pointed at a fixed azimuth and elevation and observes a narrow strip as the sky drifts past. In practice, to enable re-observation of strips as necessary, the telescope is driven very slowly to maintain a constant J2000 declination. In order to perform phase calibration, bright nearby point sources selected from the Very Long Baseline Array Calibrator Survey (VCS; Beasley et al. 2002) were observed for 400 seconds at 30-minute intervals during each scan. Strips are observed at a separation of 12 arcmin in δ , corresponding to the 35% point of the power primary beam, i.e. at distance x from the centre where $\exp(-x^2/(2\sigma^2)) = 0.35$, assuming the beam is Gaussian with width σ . This produces a very even noise level across the combined map, with a variation of $\approx 3\%$ between the centre of a declination strip and the point halfway between declination strips. The noise level in the survey is ≈ 3 mJy beam $^{-1}$ away from bright sources and is as low as ≈ 1 mJy beam $^{-1}$ at some points.

This data release consists of observations above $\delta = 40^\circ$ and between $b \approx \pm 5^\circ$; a later data release will extend the coverage to $\delta \geq 20^\circ$, corresponding to $53^\circ \lesssim \ell \lesssim 76^\circ$ and $170^\circ \lesssim \ell \lesssim 193^\circ$. The coverages of some other, currently available Galactic plane surveys along with their resolutions and noise levels are shown in Table 1, and some of these are illustrated in comparison to the (full) AMIGPS in Fig. 1. The AMIGPS is the first survey at this frequency to achieve similar coverage area, resolution and noise level to lower frequency surveys such as the Canadian Galactic Plane Survey (CGPS; Taylor et al. 2003); earlier surveys have either been wide and shallow with lower resolution (e.g. the GPA), or narrower, with comparable resolution but still more shallow than the AMIGPS (e.g. Nobeyama at 10 GHz; Handa et al. 1987).

The observations for the first data release were performed between 22 Jun 2010 and 4 Nov 2011. Approximately two thirds of the strips were observed multiple times in order to improve the noise level, resulting in a total observing time of ≈ 1200 hours.

4 DATA REDUCTION AND MAPPING

Data reduction was performed using the local software tool `REDUCE`, which flags interference, shadowing and hardware errors, applies phase and amplitude calibrations, and Fourier transforms the lag correlator data to synthesize the frequency channels, before outputting to disc in `uv`-`FITS` format. Flux calibration was performed using short observations of 3C48, 3C286 or 3C147 near the beginning and end of each run. The assumed flux densities for

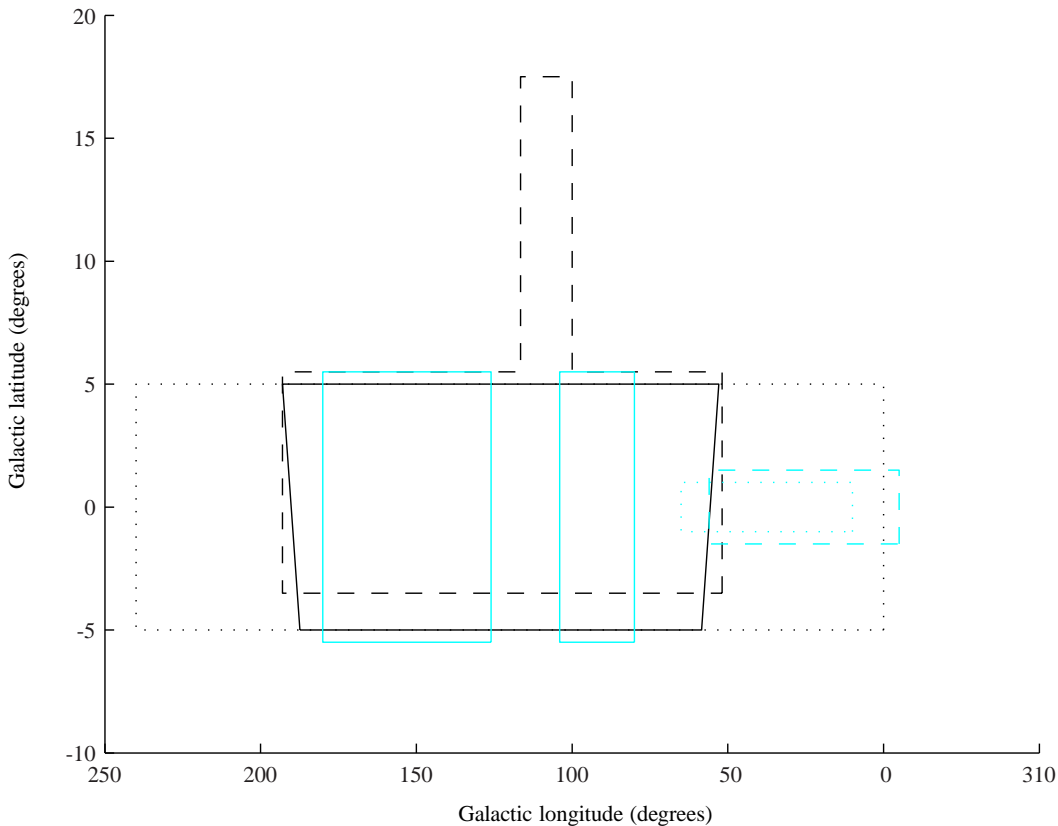


Figure 1. Coverage of the full AMIGPS compared to other northern Galactic plane surveys of similar area and/or resolution and noise level. The AMIGPS boundaries are shown as a solid black line, CGPS (408, 1420 MHz) as a dashed black line, Effelsberg (1.4, 2.7 GHz) as a dotted black line, 7C(G) (151 MHz) as a solid cyan line, Nobeyama (10 GHz) as a dashed cyan line, and CORNISH (5 GHz) as a dotted cyan line.

3C286 were calculated from Very Large Array total-intensity measurements provided by R. Perley (private communication), and are consistent with the Rudy et al. (1987) model of Mars transferred onto absolute scale, using results from the *Wilkinson Microwave Anisotropy Probe* satellite. The assumed flux densities for 3C48 and 3C147 are based on long-term monitoring with the AMI SA using 3C286 for flux calibration (see Table 2). A correction for each antenna for changing weather and radiometer performance is also applied using a noise-injection system, the ‘rain gauge’ (see AMI Consortium: Zwart et al. 2008 for more details).

Many of the automatic flagging routines used to excise interference from AMI data rely on the amplitude of the astronomical source being observed remaining constant throughout the observation. This is not the case for drift-scan data, where sources drift through the primary beam. It was found that the automated routines (designed in particular to remove interference spikes) were partially flagging out bright sources, so that their flux densities measured from the final maps were systematically lower than expected compared to flux densities from tracked observations. To overcome this, an iterative scheme was introduced in which the data are reduced as usual, then the visibility data are averaged over channels and baselines and searched for remaining peaks, indicating the presence of a bright source. The data are then re-reduced, with the time ranges within which bright sources are found being excluded from the interference flagging routines.

In order to process the continuous drift-scans, pointing centres were set up spaced 10 arcmin apart in RA and each sample was phase-rotated to the closest pointing centre. The SA integration time is one second, so this results in $600/(15 \cos(\delta))$ samples per pointing centre, which yields approximately 70 samples at $\delta = 55^\circ$. The data were then exported in multi-source *uv*-FITS format. The in-house software package FUSE was used to concatenate visibility data from different observations of the same declination strip, weighting each observation according to its noise level; variability of sources has not been considered (see Section 6.2).

4.1 Mapping

The pointings were imaged separately in AIPS¹ with 128×128 pixel maps, where the pixels are 20×20 arcsec 2 in size. Natural weighting was used to maximise signal-to-noise, and all six frequency channels were imaged using a multi-frequency synthesis; as a consequence of different flagging of the channels, the effective frequency will vary slightly between pointings. Individual channel maps were not produced. An automated CLEANING process was used to place a 6×6 pixel CLEAN box around the brightest pixel if it had a flux density greater than 200 mJy, and the images were CLEANED to three

¹ ASTRONOMICAL IMAGE PROCESSING SYSTEM – www.aips.nrao.edu/

Table 1. Coverage, resolution and noise levels of selected Galactic plane surveys. The noise level marked with (*) is actually a detection limit.

Telescope/ Survey name	Frequency (GHz)	Coverage (deg ²)	Resolution (arcmin)	Noise level (mJy beam ⁻¹)
7C(G) ^a	0.151	1700	1.17 cosec(δ)	40
AT20G ^b	20	20086	1.7	10
CGPS ^c	1.42	1500	1 cosec(δ)	0.23
	0.408		3.4 cosec(δ)	3
CORNISH ^d	5	110	0.017	0.4
	4.875 ^e	125	2.6	120(*)
Effelsberg	1.4 ^{f,g}	2400	9.3	80
	2.7 ^{h,i}		4.3	50
GPA ^j	8.35	2700	10	230
	14.35		7	800
MAGPIS ^k	1.42	43.2	0.083	0.2
Nobeyama ^l	10	183	3	33
	0.96		4 \times 75	60
RATAN ^m	3.9	400	1 \times 39	10
	11.2		0.35 \times 14	100
Stockert ⁿ	2.72	10200	18	140
VGPS ^o	1.42	< 200	1	2
VLA	5 ^p	40	0.07	2.5–10
	1.42 ^q	224	0.07	10
VSA ^r	30	152	13	90

^a Vessey & Green (1998); ^b Murphy et al. (2010); ^c Taylor et al. (2003);

^d Purcell, Hoare, & Diamond (2008); ^e Altenhoff et al. (1979);

^f Reich, Reich, & Fürst (1990); ^g Reich, Reich, & Fürst (1997);

^h Reich et al. (1984); ⁱ Reich et al. (1990); ^j Langston et al. (2000);

^k Helfand et al. (2006); ^l Handa et al. (1987); ^m Trushkin (1998);

ⁿ Reif et al. (1987); ^o Stil et al. (2006); ^p Becker et al. (1994);

^q Zonematkermani et al. (1990); ^r Todorović et al. (2010)

Table 2. Assumed I + Q flux densities of 3C286, 3C48 and 3C147.

Channel	$\bar{\nu}$ /GHz	S^{3C286} /Jy	S^{3C48} /Jy	S^{3C147} /Jy
3	13.88	3.74	1.89	2.72
4	14.63	3.60	1.78	2.58
5	15.38	3.47	1.68	2.45
6	16.13	3.35	1.60	2.34
7	16.88	3.24	1.52	2.23
8	17.63	3.14	1.45	2.13

times the r.m.s. noise on the dirty image; the box was removed, and the CLEANING was continued to the same flux density level. Each component map was CLEANED using an elliptical Gaussian fitted to the central region of the dirty beam as the restoring beam. As a result, the restoring beam for each component map is slightly different. The distribution of synthesised beam sizes is shown in Fig. 2.

The noise on each component map was estimated using the IMEAN task over the whole map, which fits a Gaussian centred on zero to the distribution of pixel values, discarding outliers. Fig. 3 shows a typical beam-corrected pointing map at $\delta \approx 55^\circ$ with its restoring beam, along with the uv -coverage for the pointing centre.

4.2 Primary-beam correction

The SA primary beam is usually approximated by a Gaussian fitted to the central lobe of the beam, with a FWHM of 19.6 arcmin at the

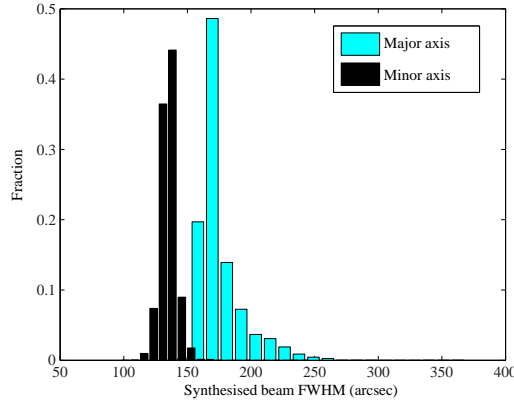


Figure 2. The distribution of synthesised beam major and axis FWHMs for the pointing centres which make up the drift-scan maps.

central frequency. However, primary beam correction of drift-scan maps is complicated due to the continuous nature of the scan: each pointing does not consist solely of data taken towards its centre, but rather of data taken towards a series of points along its RA axis, corresponding to data taken at different times. The primary beam was therefore calculated as a weighted average of beams centred at each of the constituent points, i.e. for any pixel in the map

$$\text{primary beam} = \frac{\sum_{i=1}^N w_i \exp\left(-\frac{\Delta_i^2}{2\sigma^2}\right)}{\sum_{i=1}^N w_i} = \frac{\sum_{i=1}^N w_i \exp\left(-\frac{(x-x_i)^2+y^2}{2\sigma^2}\right)}{\sum_{i=1}^N w_i}, \quad (1)$$

where N is the number of samples constituting the pointing, $w_i = 1/\sigma_{\text{rms},i}^2$ is the weight of the i 'th sample (i.e. the sum of weights for all baselines and all channels contributing to a one-second sample) where $\sigma_{\text{rms},i}$ is the r.m.s. noise on the sample, $2\sigma \sqrt{2\ln(2)}$ is the FWHM of the SA primary beam (19.6 arcmin), and $\Delta_i = \sqrt{(x-x_i)^2 + y^2}$ is the separation of the pixel from the pointing centre of the sample, where (x, y) is the pixel location and $(x_i, 0)$ is the pointing centre of the sample along the RA axis. The pixel value is then divided by the weighted-average beam for that pixel; pixels with a weighted-average beam of ≤ 0.1 are blanked. This has the effect of elongating the beam along the RA axis compared to the normal SA primary beam correction; this is illustrated in Fig. 4.

This beam correction was applied to each of the individual pointing maps outputted from AIPS and a noise map for each pointing was also produced, which is the inverse of the primary beam scaled by the r.m.s. noise value of the map outputted from IMEAN.

4.3 Map combination

Finally, the individual beam-corrected pointing maps were added together, weighting each pixel by the inverse of its variance calculated from the noise map, into larger continuous maps using the in-house software PROFILE (Grainge et al. 2002). Corresponding continuous noise maps for use in source-finding were also produced in the same way from the noise maps for the individual pointing centres; these are found to provide an accurate representation of the noise, except around bright sources as discussed in Section 5.2.

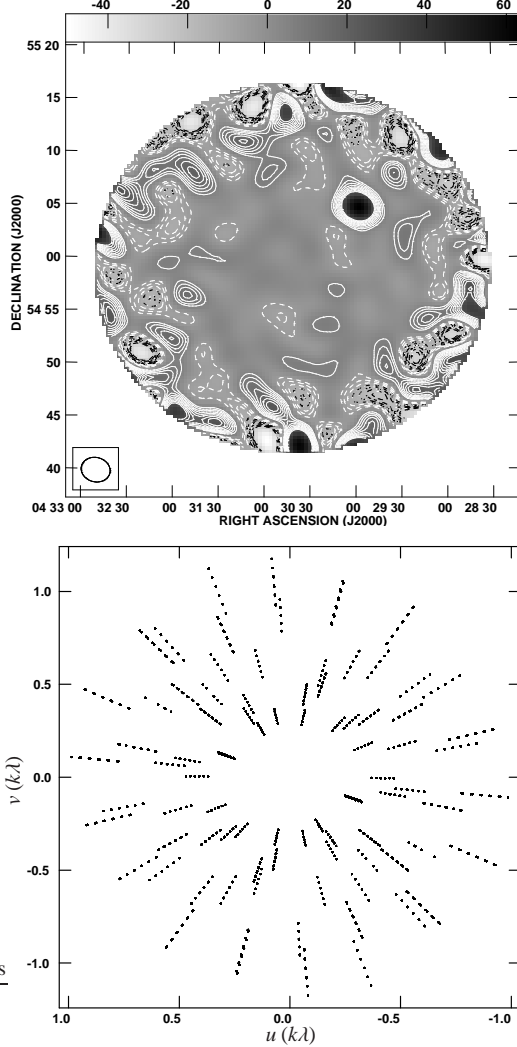


Figure 3. The beam-corrected map (top) and uv -coverage (bottom) for a typical drift-scan pointing centre at $\delta \approx 55^\circ$. The 1σ map noise at the centre of the map is $2.72 \text{ mJy beam}^{-1}$, as estimated by IMEAN; the noise increases away from the centre (up to a factor of ten). The map has contours at ± 2 – 10σ ; solid contours are positive and dashed contours are negative. The synthesised beam is shown in the bottom left-hand corner. The grey-scale is in units of mJy beam^{-1} .

Fig. 5 shows an example noise map section illustrating the variation in noise level across a typical map. All maps were also regridded into Galactic co-ordinates using the AIPS task REGRD.

5 SOURCE EXTRACTION

AMI Consortium: Franzen et al. (2011) describes the source extraction methodology used for the 10C survey; a similar process was used for the AMIGPS. Source finding was carried out over the combined maps to search for peaks greater than 5σ , where σ is the r.m.s. noise value read from the corresponding pixel on the noise map. A peak position and flux density value is measured by interpolating between the grid points. An initial estimate of the integrated flux density and source size is also calculated by integrating contiguous pixels down to $2.5 \times$ the local thermal noise level, and sources are identified as overlapping if the integration area contains

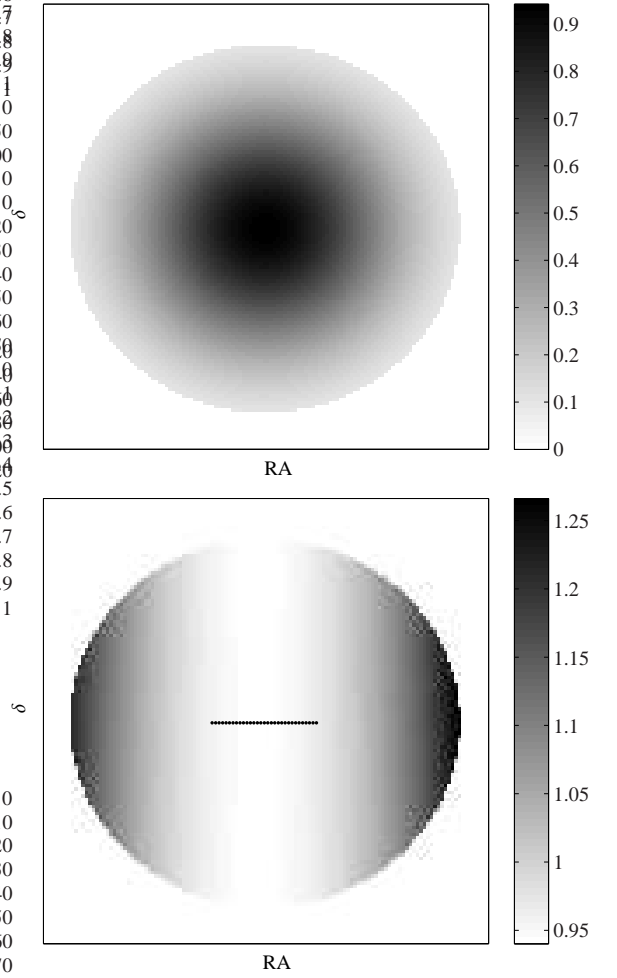


Figure 4. An example of the drift-scan primary beam. This is the weighted average of the SA primary beam centred at each of the samples taken along the RA axis. The figure on the top shows the weighted-average primary beam for the same pointing shown in Fig. 3; the bottom figure shows the weighted-average primary beam divided by the usual SA primary beam for a typical, non-drift-scan pointing. The coordinates of the samples constituting the pointing are overplotted in black. The diameter in RA of the pointing is ≈ 37 arcmin, whereas the diameter of a typical, non-drift-scan pointing cut off at the 10% point is ≈ 35 arcmin.

more than one peak $> 5\sigma$. This information is used to fit an elliptical Gaussian to each source in an automated fashion, using the AIPS task JMFIT. Overlapping sources are fitted simultaneously. As JMFIT can only fit up to four sources simultaneously, in a limited number of cases where more than four sources were identified as overlapping by the source-finding software sources were regrouped manually into groups of four or less.

5.1 Source size and classification

The deconvolved source size is calculated by JMFIT using the synthesised beam size at the pointing with the highest weight at the position of the source. This size is used to classify the source as point-like or extended to the SA beam, following the method described in AMI Consortium: Franzen et al. (2011), scaled to the SA beam size. A source is classified as extended if the fitted major axis

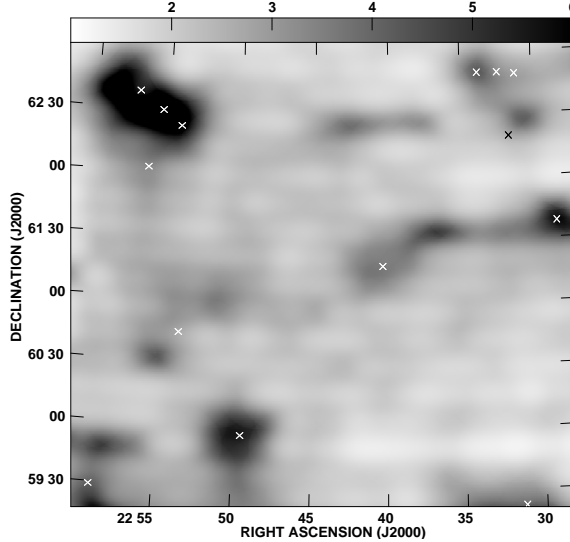


Figure 5. A typical noise map illustrating the variation in noise level across the map. The grey-scale is in mJy beam^{-1} and is truncated at 6 mJy beam^{-1} to show the low-level variation; the highest noise level in the area shown is $\approx 10 \text{ mJy beam}^{-1}$ in the north-eastern corner. Crosses mark the positions of sources with peak flux densities $> 50 \text{ mJy beam}^{-1}$, around which it can be seen that the noise level increases. Away from the bright sources, the noise level is $\lesssim 3 \text{ mJy beam}^{-1}$.

size $e_{\text{maj}} \geq e_{\text{crit}}$, where

$$e_{\text{crit}} = \begin{cases} 3.0b_{\text{maj}}\rho^{-1/2} & \text{if } 3.0b_{\text{maj}}\rho^{-1/2} > 100.0 \text{ arcsec}, \\ 100.0 \text{ arcsec} & \text{otherwise,} \end{cases} \quad (2)$$

where ρ is the signal-to-noise ratio and b_{maj} is the synthesised-beam major-axis size.

If a source is classified as extended, its integrated flux density outputted from JMFIT is considered to best represent its total flux density; otherwise the peak flux density is considered to provide a more accurate measurement.

The error inherent in using the beam from the pointing with the highest weight at the position of the source for source extraction has been investigated by remapping a section of the survey with identical restoring beams for all pointing centres. The flux densities derived from this map were compared with the catalogue values for sources which lie between pointing centres with different beam shapes and sizes. For point-like sources, the difference in the flux density is $\lesssim 1\%$ and is considered to be negligible. For extended sources it is $\lesssim 5\%$, so a conservative extra 5% error on the flux density is added in quadrature (see Section 6.2).

Although a Gaussian is a reasonable approximation to the shape of many sources, clearly in the Galactic plane there are many sources which are not Gaussian in shape. Integrated flux densities should therefore be used with caution. The ' χ^2 ' statistic (actually the sum of squared residuals) outputted from JMFIT is included in the catalogue as an indication of the goodness of fit. It should be noted that integrated flux densities will also be affected by flux loss when the source is extended on scales that are large compared to the SA synthesised beam.

5.2 Spurious source exclusion

An implausibly large number of sources are frequently detected in the vicinity of bright sources – these are likely spurious and

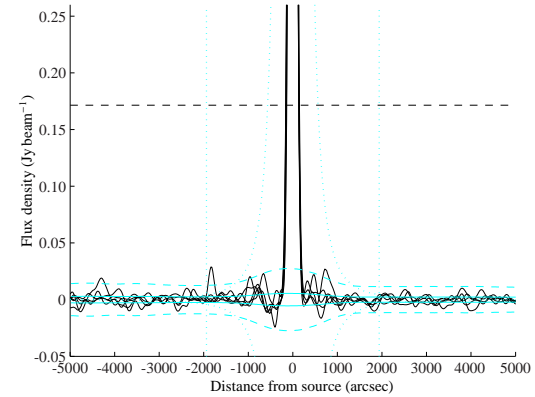


Figure 6. Pixel values (solid black lines) interpolated through map points in lines intersecting the bright, central source in Fig. 7, and the spurious sources around it; the mean noise- and 5σ -detection-levels (solid and dashed cyan lines) from the noise map; the fall-off law and exclusion zone radius for this source (cyan curved and vertical dotted lines); and the $S_{\text{peak,bright}}/10$ cutoff line (dashed black line). It can be seen that the noise outside the exclusion zones is well represented by the map noise, however closer to the central source the noise is elevated and the 5σ cutoff is not high enough. The conservative $S_{\text{peak,bright}}/10$ cutoff excludes the spurious detections.

are caused by residual amplitude and phase errors in the data and unCLEANed sidelobes. In order to prevent these from contaminating the catalogue, ‘exclusion zones’ were applied to sources with peak flux density $> 50 \text{ mJy beam}^{-1}$. The radii r_E of the exclusion zones are determined by the peak flux density $S_{\text{peak,bright}}$ of the source as $r_E = 18(S_{\text{peak,bright}}/300 \text{ mJy})^{1/3}$ arcmin. This was chosen empirically to describe the fall-off in the elevated, non-Gaussian noise around bright sources, illustrated in Fig. 6. Within the exclusion zones, only ‘sources’ with peak flux density $S_{\text{peak}} \geq S_{\text{peak,bright}}/10$ are retained. The factor of ten was conservatively chosen by eye to retain most of the sources which appear to be real, while excluding as many spurious sources as possible. There may be some real sources which are excluded by this procedure; the implications of this for the completeness of the catalogue will be discussed in Paper II. Fig. 7 illustrates the exclusion zones around two bright sources.

6 CALIBRATION ACCURACY CHECKS

As many bright sources found in the Galactic plane are well known and frequently used as phase-calibrator sources by AMI, it is possible to use them to check both the positional and flux calibration accuracy of the drift-scan survey. A follow-up campaign with the AMI LA has also been conducted on sources identified as having rising spectra with respect to the NVSS (Condon et al. 1998) (this will be described in detail in Paper II). Since the positional accuracy of the LA is much greater than that of the SA (the synthesised beam is ≈ 30 arcsec), these pointed follow-up observations provide an additional check on the calibration accuracy.

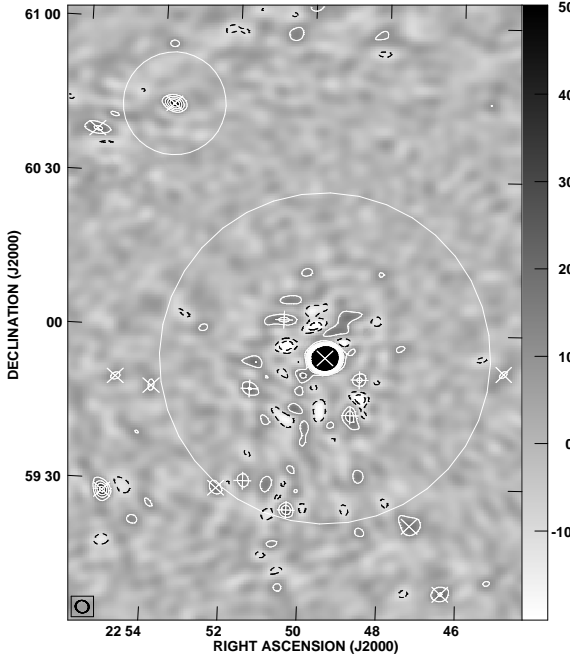


Figure 7. A section of the map illustrating the spurious source exclusion method. The grey-scale is in mJy beam^{-1} and is truncated to show the fainter sources; the flux densities of the brightest and second brightest sources are $\approx 1700 \text{ mJy}$ and 50 mJy respectively. The contour levels are between $\pm 100 \text{ mJy beam}^{-1}$ in steps of 10 mJy beam^{-1} (it is not possible to use σ contours since the noise level varies across the map); solid contours are positive and dashed contours are negative. Exclusion zones are shown as circles around the bright sources. Source detections are marked by \times , and ‘sources’ detected but excluded by $+$. The synthesised beam at the position of the brightest source is shown in the bottom left hand corner.

6.1 Positional accuracy

6.1.1 Point-like sources

The catalogue of source positions (for point-like sources only) derived from the survey maps was matched to the milliarcsecond-accurate positions from the VCS catalogue (Beasley et al. 2002), resulting in 125 matches with signal-to-noise ratio (SNR) in the drift-scan maps ranging from ≈ 8 to 600. In addition, the positions derived from follow-up observations of objects that were also point-like to the LA were compared to the drift-scan catalogue positions, resulting in 270 additional matches (not matched to a VCS source) with SNR in the drift-scan maps ranging from ≈ 5 to 400.

The errors σ_{RA} and σ_{δ} in RA and δ for a point source are assumed to be given by

$$\sigma_{\text{RA}}^2 = \epsilon_{\text{RA}}^2 + \sigma_{\text{M}}^2 \sin^2(\phi) + \sigma_{\text{m}}^2 \cos^2(\phi) \quad (3a)$$

$$\sigma_{\delta}^2 = \epsilon_{\delta}^2 + \sigma_{\text{M}}^2 \cos^2(\phi) + \sigma_{\text{m}}^2 \sin^2(\phi), \quad (3b)$$

where $\epsilon_{\text{RA or } \delta}$ are the r.m.s. calibration errors in RA and δ , $\sigma_{\text{M or m}}$ are the noiselike uncertainties parallel to the synthesised beam major (M) and minor (m) axes, and ϕ is the position angle of the beam. We assume the noiselike uncertainties are given by

$$\sigma_{\text{M or m}} = \frac{\theta_{\text{M or m}}}{\sqrt{2 \ln(2)} \text{ SNR}}, \quad (4)$$

where $\theta_{\text{M or m}}$ are the major and minor FWHM of the synthesised beam.

To test for systematic RA and δ offsets, the mean offsets between both the AMIGPS and VCS catalogue and AMIGPS and LA

Table 3. Mean RA and δ position offsets for high SNR sources in the drift-scan catalogue (all in arcsec). Consistency is checked by using the offsets from VCS catalogue and LA positions separately, and combined, and by changing the minimum SNR.

SNR limit	Offset from	Number of sources	Mean RA offset	Mean δ offset
50	VCS	56	0.9 ± 0.5	-0.4 ± 0.3
	LA	18	-1.1 ± 0.7	-0.9 ± 0.7
	Combined	74	0.5 ± 0.4	-0.5 ± 0.3
100	VCS	30	0.6 ± 0.7	-0.6 ± 0.4
	LA	5	-0.5 ± 1.5	-1.0 ± 1.0
	Combined	35	0.5 ± 0.4	-0.65 ± 0.3

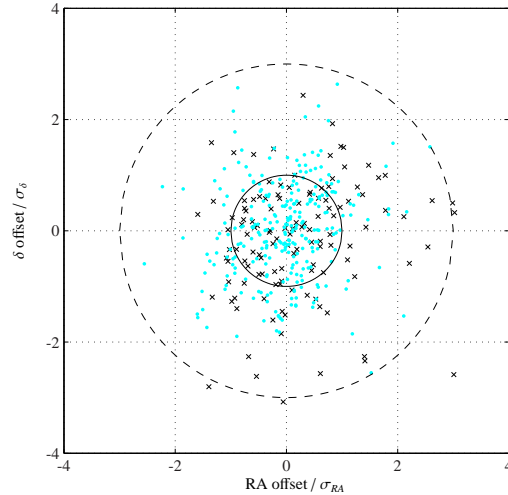


Figure 8. RA and δ offsets normalised by their calculated errors for all sources which are matched to a VCS source with well-known position (black crosses) or have been followed up with the LA (cyan dots). The estimated 1 and 3σ error circles are also shown.

positions were calculated separately and as a single group, and by selecting sources with $\text{SNR} > 50$ and $\text{SNR} > 100$ in the drift-scan maps. These are listed in Table 3, and are all consistent with zero within $< 2.5\sigma$, so we assume no systematic offset in RA or δ .

To determine the r.m.s. calibration errors, ϵ_{RA} and ϵ_{δ} were varied until 99.7% of the sources with VCS positions had offsets within 3σ calculated from Equation 3. This gave $\epsilon_{\text{RA}} = 2.6 \text{ arcsec}$ and $\epsilon_{\delta} = 1.7 \text{ arcsec}$. Fig. 8 shows the positional offsets for all sources in both datasets, normalised by the calculated error. They agree well, with 99% of all offsets lying within the 3σ circle (the statistics are only approximately Gaussian).

6.1.2 Extended sources

For sources that are extended given the SA beam, the positional uncertainty is calculated slightly differently. The errors in RA and δ are given by

$$\sigma_{\text{RA}}^2 = \epsilon_{\text{RA}}^2 + \sigma_{\text{J,RA}}^2 \quad (5a)$$

$$\sigma_{\delta}^2 = \epsilon_{\delta}^2 + \sigma_{\text{J,}\delta}^2, \quad (5b)$$

where the $\sigma_{J,RA}$ or J,δ terms are the errors outputted by the AIPS fitting task JMFIT, which folds in an estimate of the noiselike error as well as the error associated with the fit.

6.2 Flux calibration accuracy

We assume flux calibration errors are given by

$$\sigma_{S_{\text{peak}}}^2 = (0.05 S_{\text{peak}})^2 + \sigma^2 \quad \text{for a point-like source} \quad (6a)$$

$$\sigma_{S_{\text{int}}}^2 = 2(0.05 S_{\text{int}})^2 + \sigma^2 \quad \text{for an extended source,} \quad (6b)$$

where S_{peak} is peak flux density and S_{int} is integrated flux density. This error estimation comprises a 5% calibration uncertainty (including rain-gauge correction) and a noise-like error σ which for a point-like source is the r.m.s map noise measured from the CLEANED map, and for an extended source is the error outputted from JMFIT which also folds in an estimation of the fitting error. The error for an extended source also contains an extra 5% error due to the uncertainty in the beam shape, as discussed in Section 5.

At 16 GHz, intrinsic source variability is important. AMI Consortium: Franzen et al. (2009) find that of 93 extragalactic sources monitored with the AMI SA for periods between one and 18 months, $\approx 50\%$ are variable above the flux density calibration uncertainties and 15% are variable at a level of more than 20%. Variability must therefore be considered when attempting to test the flux calibration accuracy.

6.2.1 NGC 7027

NGC 7027 is a planetary nebula lying within the drift-scan survey area and for present purposes essentially non-variable (see, e.g. Zijlstra, van Hoof, & Perley 2008). It is also frequently monitored by AMI with tracked observations so an accurate flux density at 16 GHz can be calculated for comparison. Using data taken between 2007 and July 2012 with the SA, the 16 GHz flux of NGC 7027 is 5.4 Jy. The drift-scan flux for NGC 7027 is 5.1 ± 0.3 Jy, agreeing with the tracked value to within 1.2σ .

6.2.2 3C48

3C48 is one of the primary calibration sources used by AMI and is also known to be non-variable. Separate drift-scan observations were made of an area around it between Mar and Dec 2010 as an initial test of the drift-scan pipeline. These observations were reduced both in the standard pipeline, which uses the closest primary calibrator observations in time including 3C48, as well as using only 3C286 as a primary calibrator. 3C48 has a flux density of 1.64 Jy at 16 GHz; the drift-scan flux density is 1.60 ± 0.08 Jy, using 3C48 and 3C286 as primary calibrators, and 1.63 ± 0.08 Jy using only 3C286. Both values are consistent with each other and are within 0.5σ of the nominal value.

6.2.3 Concurrent observations

Since AMI is continually observing phase calibrators for many of its observations, there is a high probability of quasi-simultaneous tracked observations existing of bright compact sources, mostly extra-galactic, seen in the drift-scan survey. Extrapolating from Fig. 3 of AMI Consortium: Franzen et al. (2009) which shows the variability index for extra-galactic sources at 15 GHz as a function of time, 10 days was chosen as an interval within which source

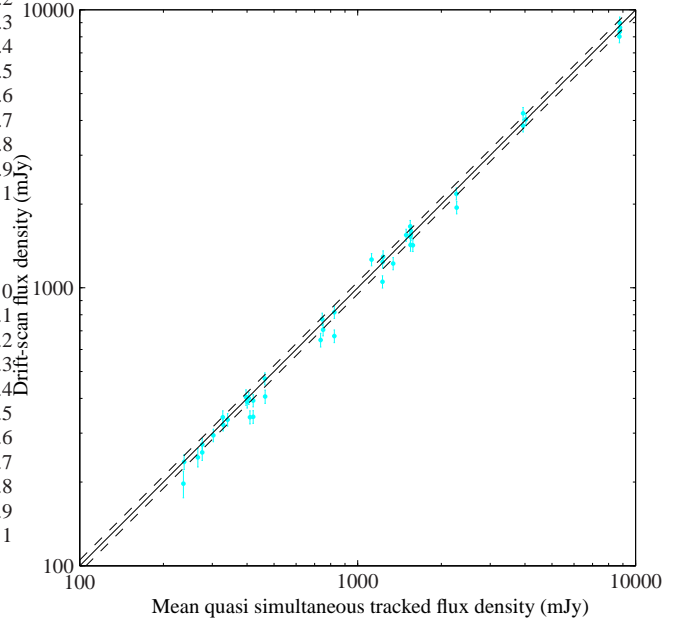


Figure 9. Drift-scan flux densities compared to the mean flux from tracked SA archival observations within 10 days. The black solid and dotted lines show a one-to-one correspondence and $\pm 5\%$ flux-calibration uncertainty.

variability should be small. Since the drift-scan survey also consists of multiple observations at different dates, each observation which contained a potential match within ± 10 days was reimaged separately and source-finding was done on the individual declination strips. Any archival SA tracked observations within ± 10 days of drift observations of matching sources were averaged and compared with the individual drift-scan values. Fig. 9 illustrates the comparison between the peak flux densities of these sources; 93% of the drift-scan flux densities are within 3σ of the mean archival flux.

The three outliers had lower drift-scan flux densities than the mean archival flux density and were found to lie near the edge of the declination strip, where phase errors are expected to have the greatest effect. In each case, the source appears near the centre of the adjacent strip, which was observed a day later. When creating the final combined map, the pixels nearer the centre of individual pointings are given greater weight, so the discrepant flux densities will be down-weighted. The flux densities for these sources derived from raster maps produced from observations close in time agree with the mean archival flux to within 1σ .

It is common for survey flux densities to be slightly suppressed due to small phase errors shifting the positions of sources which lie away from the pointing centres in the constituent maps (see, e.g. AMI Consortium: Davies et al. 2011). The concurrent observations were tested for this effect, but the median percentage difference $((S_{\text{mean,tracked}} - S_{\text{drift}})/S_{\text{mean,tracked}})$ was found to be only $\approx 2\%$, so the AMIGPS flux densities were not adjusted for this effect.

6.2.4 Non-concurrent observations

A final check of the flux calibration accuracy can be made by comparing the LA follow-up flux densities to the drift-scan flux densities for sources that are found to be point-like to the LA, although these observations are widely spaced in time (by up to ≈ 1.5 years). Very little is known about variability statistics in the

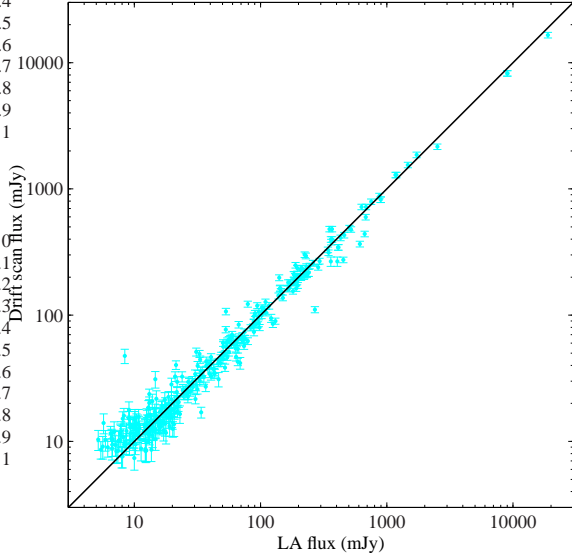


Figure 10. Drift-scan flux densities compared to the LA follow-up flux. The black solid line shows a one-to-one correspondence.

Galactic plane at cm-wavelength. However, some idea of the expected number of variable sources can be obtained using results from the 5-GHz Galactic plane variability study by (Becker et al. 2010), where $\approx 8\%$ of sources detected in the flux density range from 1 – 100 mJy between $b \approx \pm 1.0^\circ$ were found to be variable on a time scale of years or shorter when no correction for the inclusion of the extra-galactic source population was applied.

Fig. 10 shows the comparison between the LA and drift-scan survey peak flux densities. 87% are within 3σ , taking into account the LA errors which are generally smaller than the drift-scan errors and are not plotted for clarity. The remaining 13% seems consistent with the 8% of sources predicted to be variable, given that no correction for differences in frequency, flux density range, Galactic latitude distribution or bias due to selecting for rising spectrum sources has been attempted. The apparent bias towards higher drift-scan flux densities at the lower end of the flux density scale is likely an Eddington bias caused by low-SNR sources selected from the AMIGPS map being more likely to occur on positive noise bumps.

7 DATA PRODUCTS

7.1 Raster maps

The field is divided into 38 square maps of side 6° , and are given names constructed from the Galactic coordinates of their centres, eg G78.0–2.2. These are shown in Fig. 11. The centres are spaced by 5° in longitude, and 4.4° in latitude, and start at $\ell = 78.0^\circ$, $b = -2.2^\circ$.

These raster maps, along with the corresponding noise maps, are available from <http://www.mrao.cam.ac.uk/surveys/AMIGPS/>. Also included with the maps as an extra `fits` data-cube are tables giving the synthesised beam sizes appropriate to each pixel (i.e. the synthesised beam belonging to the pointing with the highest weight at that pixel).

Fig. 12 shows an example 6 deg^2 map, with annotations marking the sources detected within it. Also shown for comparison is a CGPS total intensity 1.4 GHz map showing the same region. It can be seen that many sources detected by CGPS are also detected

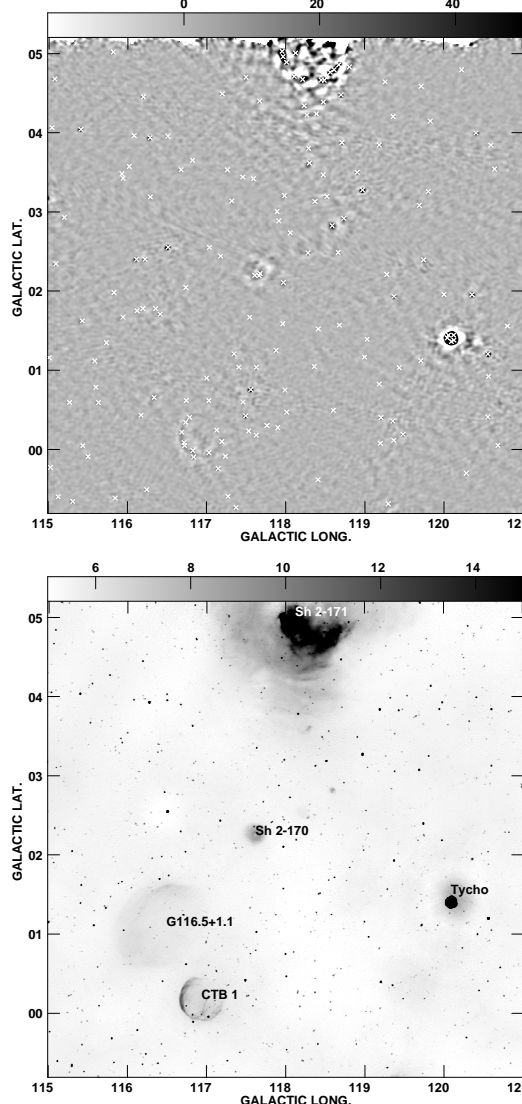


Figure 12. An example AMIGPS raster map centred at $\ell = 118.0^\circ$, $b = 2.2^\circ$ (top) and the corresponding CGPS total intensity map at 1.4 GHz (bottom). The AMIGPS map has source detections marked with \times ; the grey-scale is in mJy beam^{-1} and is truncated at -20 and $+50 \text{ mJy beam}^{-1}$ to show the fainter features. The grey-scale of the CGPS map is in K and is truncated at 15 K for the same reason. Some well-known supernova remnants (SNR) and HII regions visible in the map are labelled (Green 2009, Sharpless 1959). It can be seen that the AMIGPS sees many features common to the CGPS, however the larger-scale features such as the SNR G116.5+1.1 are resolved out.

by the AMIGPS; however some larger-scale features such as the supernova remnant G116.5+1.1 are resolved out.

7.2 Source catalogue

An abbreviated sample of the catalogue containing the first ten sources detected in Fig. 12 is shown in Table 4. The complete source list, which contains 3503 entries, is available from <http://www.mrao.cam.ac.uk/surveys/AMIGPS/>. For each source, the catalogue contains:

- A source name, constructed from the J2000 RA and δ coordinates of the source.

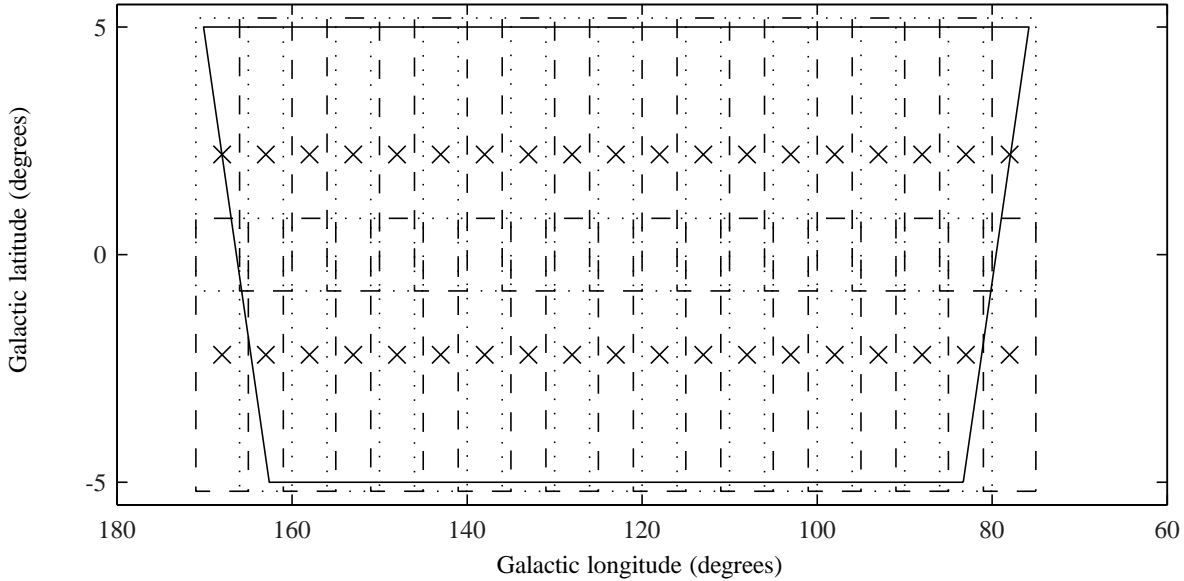


Figure 11. The positions of the raster maps in Galactic coordinates. The solid black line marks the extent of the data, the dotted and dashed lines show the boundaries of the raster maps and the crosses mark the centres of the maps.

- The peak RA, δ , flux density and associated errors (these are the appropriate quantities to use for point-like sources).
- The fitted centroid RA and δ , integrated flux density and associated errors (these are the appropriate quantities to use for extended sources).
- The critical source size as defined in Eqn. 2 and the deconvolved source major and minor axis sizes and position angle. A deconvolved size of 0.0 indicates that the source was not found to be wider than the synthesised beam in the major or minor axis direction.
- The sum of squared residuals from the fit.
- The source classification (point-like or extended).

8 CONCLUSIONS

The Galactic plane between $b \approx \pm 5^\circ$ has been surveyed using the interferometric AMI SA at ≈ 16 GHz, to a noise level of ≈ 3 mJy beam $^{-1}$ at ≈ 3 arcmin resolution. This is the most sensitive and highest resolution Galactic plane survey at cm-wave frequencies above 1.4 GHz.

(i) 868 deg 2 of the Galactic plane have been surveyed and a catalogue of 3503 sources produced. This is the first data release of the AMIGPS.

(ii) As part of creating the AMIGPS, we have developed an automated pipeline to produce maps from data taken in drift-scan mode, accounting for the presence of bright sources.

(iii) The source extraction techniques developed for the 10C survey have been applied to maps at different resolution and regions of the sky with many extended sources present.

(iv) In testing the flux calibration of the survey by comparing source flux densities derived from the AMIGPS to tracked observations of both extra-galactic and Galactic sources taken with the AMI SA and AMI LA, we find that the AMIGPS flux calibration is accurate to within 5%.

(v) The r.m.s. positional accuracy of the survey, assessed by comparing positions derived from the AMIGPS with well-known

source positions from the VLBA calibrator survey and with AMI LA follow-up positions, is 2.6 arcsec in RA and 1.7 arcsec in δ .

In a following paper the first results from the survey will be presented, and in a future data release the survey will be extended to $\delta \geq 20^\circ$.

ACKNOWLEDGMENTS

We thank the staff of the Mullard Radio Astronomy Observatory for their invaluable assistance in the commissioning and operation of AMI, which is supported by Cambridge University and the STFC. This work has made use of the distributed computation grid of the University of Cambridge (CAMGRID). This research has made use of NASA's Astrophysics Data System Bibliographic Services and the facilities of the Canadian Astronomy Data Centre operated by the National Research Council of Canada with the support of the Canadian Space Agency. The research presented in this paper has used data from the Canadian Galactic Plane Survey a Canadian project with international partners supported by the Natural Sciences and Engineering Research Council. YCP acknowledges the support of a Rutherford Foundation/CCT/Cavendish Laboratory studentship. MPS and CR acknowledge the support of STFC studentships.

REFERENCES

Altenhoff W. J., Downes D., Pauls T., Schraml J., 1979, A&AS, 35, 23
 Anglada G., 1995, RMxAC, 1, 67
 Bains I., Cohen M., Chapman J. M., Deacon R. M., Redman M. P., 2009, MNRAS, 397, 1386
 AMI Consortium: Davies, M. L., et al., 2011, MNRAS, 415, 2708
 Beasley A. J., Gordon D., Peck A. B., Petrov L., MacMillan D. S., Fomalont E. B., Ma C., 2002, ApJS, 141, 13

Table 4. An example section of the AMIGPS catalogue, containing the brightest ten sources detected in the map shown in Fig. 12. For the point-like sources, S and ΔS are peak flux densities, and for the extended source they are integrated flux densities. e_{crit} is the critical source size as defined in Eqn. 2; e_{maj} , e_{min} and e_{θ} are the deconvolved source major axis FWHM, minor axis FWHM and position angle, respectively. A FWHM of 0.0 indicates that the source was not found to be wider than the synthesised beam size. χ^2 is the sum of squared residuals from the fit.

Source	RA (J2000)	δ (J2000)	ΔRA (arcsec)	$\Delta\delta$ (arcsec)	S (mJy)	ΔS (mJy)	e_{crit} (arcsec)	e_{maj} (arcsec)	e_{min} (arcsec)	e_{θ} ($^{\circ}$)	χ^2 (mJy 2 $\times 10^3$)	Type
J001450+611744	00:14:50	+61:17:44.1	2.7	1.8	844.2	42.4	100.0	18.2	0.0	20.7	28.9	P
J235300+602850	23:53:01	+60:28:53.1	2.8	1.9	1032.2	74.3	100.0	178.5	169.6	130.3	50.7	E
J002704+595854	00:27:04	+59:58:54.0	2.8	2.0	379.6	19.2	100.0	13.8	0.0	92.6	21.5	P
J003608+585548	00:36:08	+58:55:48.4	3.8	3.5	168.6	9.1	100.0	95.0	0.0	119.4	15.7	P
J002241+604014	00:22:41	+60:40:14.1	3.3	2.5	162.6	8.5	100.0	0.0	0.0	0.0	8.20	P
J000336+630750	00:03:36	+63:07:50.9	4.0	3.1	127.7	7.0	100.0	0.0	0.0	0.0	6.24	P
J000108+605120	00:01:08	+60:51:20.3	3.9	3.1	121.4	6.6	100.0	0.0	0.0	0.0	10.9	P
J000207+605832	00:02:07	+60:58:32.5	4.8	3.9	79.7	4.6	100.0	32.3	0.0	176.2	8.66	P
J003044+590415	00:30:44	+59:04:15.6	9.2	5.8	73.7	5.1	145.8	0.0	0.0	0.0	8.78	P
J003553+595008	00:35:53	+59:50:08.6	4.6	3.7	60.9	3.4	100.0	0.0	0.0	0.0	3.80	P

Becker R. H., White R. L., Helfand D. J., Zoonematkermani S., 1994, *ApJS*, 91, 347

Becker R. H., Helfand D. J., White R. L., Proctor D. D., 2010, *AJ*, 140, 157

Casassus S., Cabrera G. F., Förster F., Pearson T. J., Readhead A. C. S., Dickinson C., 2006, *ApJ*, 639, 951

Condon J. J., Cotton W. D., Greisen E. W., Yin Q. F., Perley R. A., Taylor G. B., Broderick J. J., 1998, *AJ*, 115, 1693

Draine B. T., Lazarian A., 1998, *ApJ*, 494, L19

Draine B. T., Lazarian A., 1998, *ApJ*, 508, 157

AMI Consortium: Franzen T. M. O., et al., 2009, *MNRAS*, 400, 995

AMI Consortium: Franzen, T. M. O., et al., 2011, *MNRAS*, 415, 2699

Grainge K., Jones M. E., Pooley G., Saunders R., Edge A., Grainger W. F., Kneissl R., 2002, *MNRAS*, 333, 318

Green D. A., 2009, *BASI*, 37, 45

Handa T., Sofue Y., Nakai N., Hirabayashi H., Inoue M., 1987, *PASJ*, 39, 709

Helfand D. J., Becker R. H., White R. L., Fallon A., Tuttle S., 2006, *AJ*, 131, 2525

Langston G., Minter A., D'Addario L., Eberhardt K., Koski K., Zuber J., 2000, *AJ*, 119, 2801

Leitch E. M., Readhead A. C. S., Pearson T. J., Myers S. T., 1997, *ApJ*, 486, L23

Longair M., 1998, *ASSL*, 226, 3

Mezger P. G., Henderson A. P., 1967, *ApJ*, 147, 471

Murphy T., et al., 2010, *MNRAS*, 402, 2403

Purcell C. R., Hoare M. G., Diamond P., 2008, *ASPC*, 387, 389

Reich W., Fürst E., Haslam C. G. T., Steffen P., Reif K., 1984, *A&AS*, 58, 197

Reich W., Reich P., Fürst E., 1990, *A&AS*, 83, 539

Reich W., Fürst E., Reich P., Reif K., 1990, *A&AS*, 85, 633

Reich P., Reich W., Fürst E., 1997, *A&AS*, 126, 413

Reif K., Reich W., Steffen P., Müller P., Weiland H., 1987, *Mitteilungen der Astronomischen Gesellschaft*, 70, 419

Rudy D. J., Muhleman D. O., Berge G. L., Jakosky B. M., Christensen P. R., 1987, *Icar*, 71, 159

Scaife A. M. M., et al., 2008, *MNRAS*, 385, 809

AMI Consortium: Scaife A. M. M., et al., 2009, *MNRAS*, 394, L46

Scaife A. M. M., et al., 2010, *MNRAS*, 403, L46

Sharpless S., 1959, *ApJS*, 4, 257

Stil J. M., et al., 2006, *AJ*, 132, 1158

Taylor A. R., et al., 2003, *AJ*, 125, 3145

Tibbs C. T., et al., 2011, *MNRAS*, 418, 1889

Todorović M., et al., 2010, *MNRAS*, 406, 1629

Trushkin S. A., 1998, *IAUS*, 179, 103

Vessey S. J., Green D. A., 1998, *MNRAS*, 294, 607

Waldrum E. M., Pooley G. G., Grainge K. J. B., Jones M. E., Saunders R. D. E., Scott P. F., Taylor A. C., 2003, *MNRAS*, 342, 915

Watson R. A., Rebolo R., Rubiño-Martín J. A., Hildebrandt S., Gutiérrez C. M., Fernández-Cerezo S., Hoyland R. J., Battistelli E. S., 2005, *ApJ*, 624, L89

Zijlstra A. A., van Hoof P. A. M., Perley R. A., 2008, *ApJ*, 681, 1296

Zoonematkermani S., Helfand D. J., Becker R. H., White R. L., Perley R. A., 1990, *ApJS*, 74, 181

AMI Consortium: Zwart J. T. L. et al., 2008, *MNRAS*, 391, 1545